Auto-ignition and flame stabilization of pulsed methane jets in a hot vitiated coflow studied with high-speed laser and imaging techniques

C.M. Arndt · J.D. Gounder · W. Meier · M. Aigner

Abstract The auto-ignition of a pulsed methane jet issuing into a laminar coflow of hot exhaust products of a lean premixed hydrogen/air flat flame was examined using high-speed laser and optical measurement techniques with frame rates of 5 kHz or more. OH* chemiluminescence was used to determine the downstream location of the first auto-ignition kernel as well as the stabilization height of the steady-state lifted jet flame. OH planar laser-induced fluorescence (PLIF) was used to determine further details of the auto-ignition with a higher spatial resolution. Simultaneous imaging of broadband luminosity from a viewing angle perpendicular to the OH* chemiluminescence was applied, to three-dimensionally reconstruct the ignition kernel location in space and to determine whether the first occurrence of the kernel was within or beyond the PLIF laser sheet. The development and expansion of the jet was characterized by high-speed Schlieren imaging. Statistics have been compiled for both the ignition time as well as the downstream location of the first auto-ignition kernel and the stabilization height of the steady-state lifted jet flame. From the PLIF images it was found that auto-ignition tended to occur at the interface between bulges of the inflowing jet and the coflow. For steady-state conditions, auto-ignition kernels were observed frequently below the flame base, emphasizing that the lifted jet flame is stabilized by auto-ignition.

C.M. Arndt (✉) · J.D. Gounder · W. Meier · M. Aigner
Institute of Combustion Technology, German Aerospace Center
(DLR), Pfaffenwaldring 38–40, 70569 Stuttgart, Germany
e-mail: christoph.arndt@dlr.de
Fax: +49-711-6862578

1 Introduction

Auto-ignition of fuel in a hot oxidizer plays an important role in technical devices, such as internal combustion engines, burners employing flameless combustion or reheat combustion, or scramjets. Auto-ignition in lean premixed gas turbine combustion can lead to a flame in an undesired region such as the mixing section and therefore to combustor damage [1]. Similarly, auto-ignition must also be prevented in the mixing duct of reheat combustors, where fuel is injected into the lean (diluted) exhaust products of a primary combustion stage [2–4]. In flame configurations with a recirculation zone, such as swirled flows with vortex breakdown, auto-ignition of mixtures of recirculating hot exhaust gas and fresh gas can contribute to the flame stabilization at the flame root [5].

The physical and chemical processes involved in auto-ignition are very complex and highly sensitive to boundary conditions, such as temperature, pressure, gas composition, residence time, turbulence level and strain rates [6, 7]. An excellent overview of auto-ignition, the progress in simulation of auto-ignition as well as experimental studies is given in the review paper by Mastorakos [8]. Methane auto-ignition has been studied experimentally at elevated temperature and pressure in shock tubes [9] and rapid compression machines [10] as well as in combustion bombs and flames. Because of the transiency of the phenomena and the short time scales involved, the experimental characterization of auto-ignition is quite challenging, except for very simple experimental arrangements. Auto-ignition of various fuels, such as hydrogen, acetylene and heptane, in (turbulent) hot air has been studied both experimentally [11, 12] and numerically [13, 14].

In order to study the dynamics of auto-ignition, the application of innovative high-repetition-rate laser and cam-

era systems gives the opportunity to spatially and temporally resolve the development of an ignition event and the following flame kernel development process. While most of the previous work has been performed using emission techniques such as chemiluminescence or flame luminosity imaging [1, 3, 4, 11, 16], high-speed laser measurement techniques such as planar laser induced fluorescence (PLIF) or particle image velocimetry (PIV) have only been applied in very few cases to spark ignition [17, 18] and auto-ignition [19–21].

Optical and laser-based investigations of auto-ignition in transient injection processes are found very seldom in the literature. Sadanandan et al. [19] studied the ignition of hydrogen/air mixtures by jets of hot exhaust gases. They reported that the ignition occurred near the leading edge of the jet. Bruneaux [22] reported the injection of a diesel surrogate jet into hot air at elevated pressure. He found that auto-ignition occurred in the upstream mixing zone, sometimes at multiple locations. With an increase of the injection pressure, the auto-ignition sites were shifted further downstream. The injection of a jet of gaseous dimethyl ether into a constant-pressure atmosphere was studied by Fast et al. [23]. They reported that the auto-ignition of the jet occurred over a wide spatial range. Oldenhof et al. [21] studied the pulsed injection of a natural gas jet with high-speed PIV and OH PLIF. Two cases with relatively low Reynolds numbers of 4100 and 8800 were studied. They discovered that the jet had an initial laminar phase that transitioned to a turbulent phase. No significant reactions took place before the transition to the turbulent phase.

In the present study, a pulsed methane jet is injected into a laminar flow of hot combustion products from a lean premixed hydrogen/air flat flame at atmospheric pressure. The setup is similar to the Berkeley Vitiated Coflow (BVC) Burner [24, 25]. However, previous experimental [15, 24–32] and numerical [24, 33–40] studies focused on the flame stabilization mechanism of the stably burning lifted jet flame at steady-state conditions (jet in hot coflow). From these studies it was concluded that the lifted flame is stabilized by auto-ignition. The focus of the present study however lies on the initial auto-ignition of the pulsed methane jet and the subsequent flame kernel development. Simultaneous OH planar laser-induced fluorescence, OH* chemiluminescence and broadband flame luminosity have been applied at a sustained repetition rate of 5 kHz to study the onset of auto-ignition kernels, the kernel growth and finally the development of a stable lifted jet flame. In a second set of experiments, high-speed Schlieren imaging was performed in combination with OH* and CH* chemiluminescence at a sustained repetition rate of 10 kHz in order to further characterize the jet development.
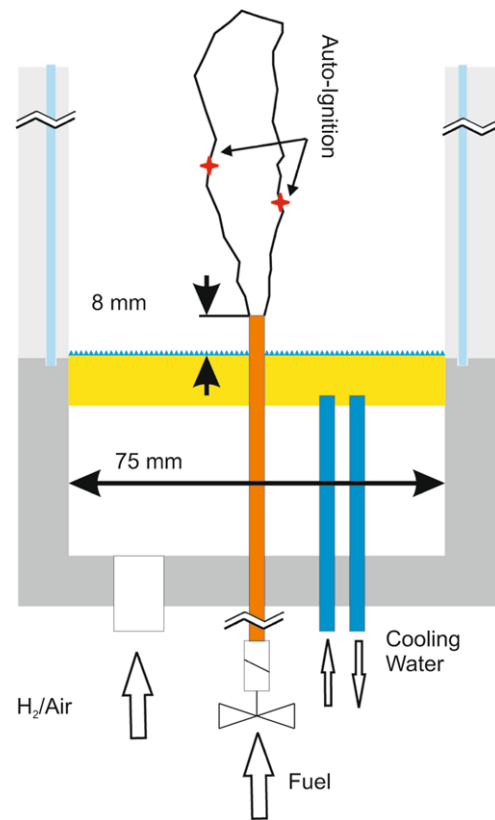

Fig. 1 Schematic drawing of the DLR Jet in Hot Coflow burner with the matrix burner and the injection system

2 Experimental

2.1 The DLR Jet in Hot Coflow burner

The DLR jet in hot coflow (JHC) burner is similar in design to the one described by Meier et al. [20], but was modified in order to achieve better boundary conditions. Figure 1 shows a schematic drawing of the burner and the fuel injector. A lean, premixed hydrogen/air flat flame was stabilized on a quadratic (75 by 75 mm^2) water-cooled bronze sinter matrix. The flame was surrounded by a square (80 by 80 mm^2) combustion chamber with a height of 120 mm to prevent any disturbance of the flow. The combustion chamber consists of four quartz glass plates, held in place by a steel post in each corner and a supporting frame at the top. This provided very good optical access for the application of laser-based and optical measurement techniques. The windows of the combustion chamber are positioned very close to the matrix in order to provide stable boundary conditions for the flat flame and the hot exhaust gas. The nozzle is a 3 mm (outer) diameter stainless steel tube (inner diameter 2 mm) through which a pulsed methane jet is injected into the vitiated coflow of the exhaust products of the flat flame. The tip of the nozzle is 8 mm above the matrix.

The burner was operated at the following operating conditions: the flow rates were 262 g min^{-1} air and 3.85 g min^{-1}

hydrogen, resulting in an equivalence ratio of $\phi = 0.505$ and an adiabatic flame temperature of $T_{ad} = 1655$ K. The adiabatic flame temperature T_{ad} was calculated for a fresh gas temperature of 298 K. The calculated exhaust gas composition at equilibrium conditions was 9.4 % O_2, 71.4 % N_2, 19.2 % H_2O and 0.03 % OH [41].

The flow rates were controlled with Brooks MFC 5850 mass flow controllers and monitored with calibration-standard Siemens Sietrans Mass 2100 Coriolis mass flow meters. The accuracy of the flow rates is within 1.5 % [42]. The uncertainty in the determination of the adiabatic flame temperature can be estimated by assuming the highest measurement uncertainty of the flow rates and calculating the adiabatic flame temperature for these cases. This resulted in an uncertainty in the order of ± 2 %. Previous measurements in a similar configuration [43] have shown that the exhaust gas of a hydrogen/air flat flame stays very close to the adiabatic flame temperature for several centimeters above the flame for cases with sufficient flow rates and thus minimized heat losses to the matrix. In order to meet this criterion, the flow rates were chosen so that the cold-flow velocities of the hydrogen/air mixture exceeded 0.7 m s^{-1}. The velocity of the hot coflow was held constant at 4 m s^{-1}.

The methane pulses were controlled with a 2/2 way spider solenoid valve (Staiger VA 204-5), located approximately 250 mm upstream of the nozzle tip. The solenoid valve received an opening trigger 2 ms after the start of each individual measurement and stayed open for 55 ms. The recording duration for each recording loop was 20 ms and thus well below the open time of the valve. At steady-state conditions, the methane jet had an exit velocity of approximately 100 m s^{-1} and a Reynolds number of approximately 13,000, as was determined with a Coriolis mass flow meter in the fuel line. Since the exit velocity of the methane pulse has a startup ramp due to the finite opening time of the solenoid valve, the exit velocity right after the valve opening was estimated from the Schlieren measurements. A steady lift-off height of the jet flame was reached a few milliseconds after the first auto-ignition event. The upper part of the nozzle became relatively hot due to the exposure to the flame. The rest of the tube was at room temperature, because the matrix was water cooled.

2.2 Planar laser-induced fluorescence (PLIF)

A sketch of the experimental setup for the OH PLIF measurements can be found in Fig. 2. The system consists of a frequency-doubled dye laser (Sirah Cobra Stretch HRR) and an intensified high-speed CMOS camera (LaVision HSS 5 with LaVision HS-IRO). The dye laser (using rhodamine 6G in ethanol) was pumped using a diode-pumped solid-state laser (Edgewave IS8II-DE). The pump laser had an average output power of 18 W at 523 nm (Nd:YLF) and a resulting
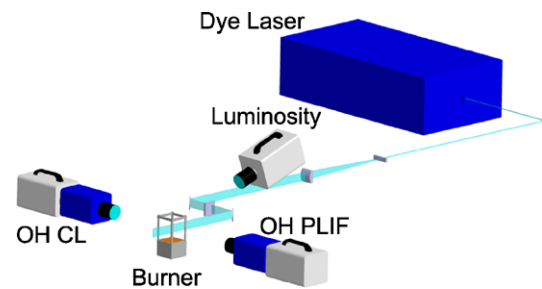

Fig. 2 Schematic of the experimental setup for the simultaneous OH PLIF, OH* chemiluminescence and broadband luminosity measurements

pulse energy of 3.6 mJ at 5 kHz repetition rate. The output radiation of the dye laser was frequency doubled to obtain laser light at 283.2 nm, in order to excite the $Q_1(7)$ transition in the A–X (1,0) band of the OH radical. The output power of the dye laser at this wavelength was 0.5 W or 0.1 mJ/pulse and the pulse duration was 9 ns. A small matrix burner with a methane–air flame was used to tune the laser to the above-mentioned transition of the OH radical.

The UV beam of the dye laser was formed into a light sheet using a two-stage cylindrical telescope, consisting of AR-coated fused silica lenses ($f_1 = -25$ mm, $f_2 = 500$ mm) and focused into the test section using a third cylindrical lens ($f_3 = 500$ mm), resulting in an approximately 43 mm-high sheet with a 0.4 mm beam waist in the test section.

The fluorescence signal was collected into the intensifier with a fast f/1.8 Cerco UV lens. Elastic scattering of the laser and broadband flame luminosity was suppressed using a high-transmission band-pass filter (>80 % transmission at 310 nm, Laser Components GmbH) and a short (200 ns) intensifier gate. Non-uniformities in the sheet profile were corrected within a post process using an average of 1000 images of the fluorescence of a uniform acetone vapor distribution in the combustion chamber.

The timing and triggering of the whole acquisition system as well as the laser was controlled with a Quantum Composers 9530 eight-channel delay generator. A SRS 945 four-channel delay generator, synchronized with the Quantum Composers 9530 delay generator, was used to provide the triggers for the cameras and the solenoid valve.

2.3 OH* and CH* chemiluminescence imaging (CL)

For the OH* and CH* CL imaging, a pair of intensified high-speed CMOS cameras (LaVision HSS 5), identical to the camera/IRO combination employed for the OH PLIF measurement, was used. Chemiluminescence of the flame was collected using fast f/1.8 45 mm Cerco UV lenses. The OH* signal was filtered using a band-pass interference filter centered around 310 nm with >80 % transmission. For the

CH* signal a band-pass filter centered around 430 nm with >45 % transmission was used.

The frame rates for the cameras were 5 kHz for the OH* CL that was acquired simultaneously with the OH PLIF and 10 kHz for the OH* and CH* CL images acquired simultaneously with the Schlieren images, as described below. The gate times of the intensifiers were set to 25 μs and 50 μs for the OH* CL and CH* CL, respectively. The active array of the cameras was set to 512 by 512 pixels^2 (for both 5 kHz and 10 kHz frame rates) in order to increase the storable amount of images in the camera memory.

2.4 Broadband flame luminosity

Broadband luminosity of the igniting jet was recorded with a LaVision HSS 6 high-speed CMOS camera, looking along the axis of the laser sheet, in order to determine the position of the first auto-ignition kernel relative to the laser light sheet (see also Fig. 2). The camera was equipped with a 50 mm f/1.4 Nikon Nikkor lens and operated at a frame rate of 5 kHz. Image acquisition started 0.6 μs after the PLIF laser pulse and simultaneously with the OH* CL camera. The exposure time of the camera was set to 200 μs and the active array of the CMOS chip was 512 by 512 pixels^2. The final field of view for the broadband luminosity camera was reduced to 30 by 70 mm^2 in the postprocessing.

The CMOS sensor of the camera is sensitive in the spectral range between 350 nm and 1100 nm. Detectable species in that spectral range include chemiluminescence from CH* and CO_2* as well as soot emission from the jet flame. Luminosity of water vapor from the exhaust gas of the flat flame was also visible in the images.

2.5 Schlieren imaging

The density variation in the test section associated with the methane pulse was visualized using a high-frame-rate Schlieren system. Collimated light from an incandescent lamp was used to illuminate the combustion chamber. Behind the combustion chamber, the collimated light beam was focused with a $f = 600$ mm spherical lens. A 500-nm long-pass filter in the beam path was used to minimize effects of chromatic aberration. An iris aperture with a 0.8 mm opening was placed in the beam focus to create the image of the density gradients.

2.6 Image postprocessing and data evaluation

One of the major challenges for optical and laser-based measurements at high repetition rates is the development of robust automated data evaluation methods that can handle the massive amount of data produced by high-speed measurements. This provides the possibility to perform statistical analysis of transient phenomena and therefore using the full potential of time-resolved data.

In the study presented here, the major goal was to perform a statistical analysis of phenomena, like the position of the first observable auto-ignition kernel, upstream and downstream propagation of the ignition kernel and lift-off height of the stably burning jet flame. This was achieved by developing a data evaluation code tailored to this specific problem in the Matlab 2007 software. An image series demonstrating the different steps of the data postprocessing is shown in Fig. 3. First, the raw images were background corrected with an average image of the coflow without the fuel jet. This corrected for most of the background luminosity. A 5 by 5 pixel^2 median filter was applied to the image to reduce noise. Then the filtered image was converted to black and white (i.e. a burnt and an unburnt gas) with an appropriate threshold (2.5 % of the maximum OH* signal intensity of the image series). Small-scale noise, for example from single-photon events on the intensifier, was filtered out by defining all areas in the thresholded images with less than 100 pixels in total as noise. Data analysis of the temporal and spatial locations of the first observed ignition kernel and the temporal development of the ignition kernel(s) was performed on the basis of those images. The ignition time as well as the lift-off height and the position of the kernel in the plane of the laser sheet were determined from the OH* CL

Fig. 3 A single shot of the OH* chemiluminescence shown at the onset of auto-ignition for various postprocessing steps: raw image, filtered and background corrected, thresholded (burned and unburnt gas). Marked in the thresholded image are the lift-off height (*LOH*), the leading edge of the flame (*LE*) and the auto-ignition location (*AI*)
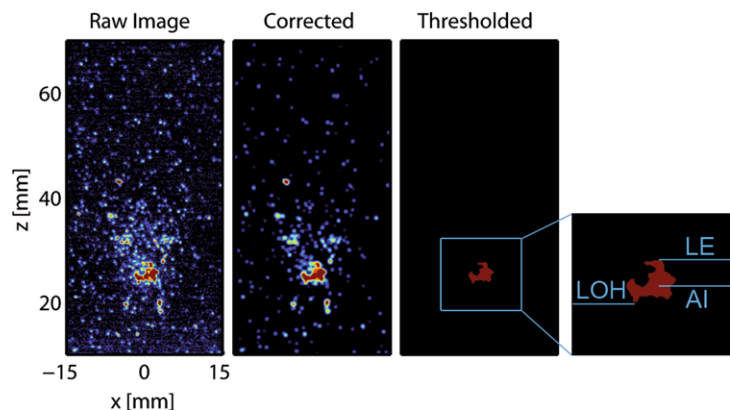
images. Also, the lift-off height of the steady-state jet flame was determined with this method.

To test the validity of this method for detecting the auto-ignition time, a second procedure to determine the auto-ignition time was applied, where the total OH* CL signal of the frame was integrated. Here, the auto-ignition time was defined as the time at which the integrated OH* CL signal intensity was greater than double the average of the noise level. Both methods worked very well in determining the ignition time, as will be described below.

As reference time for the auto-ignition time, the moment at which the jet exited the fuel nozzle was chosen. This was determined from the Schlieren images and was 2.9 ± 0.2 ms after the trigger pulse for the valve opening. The position of the ignition kernel relative to the laser sheet was determined from the broadband luminosity images. This made it possible to find ignition events that occurred inside the laser sheet for further analysis with OH PLIF. The x- and z-coordinates of the ignition kernel were defined as the centroid of the OH kernel that was detected from the thresholded OH* CL images with the axial location closest to the burner nozzle in the first frame with detected auto-ignition. The y-coordinate of the ignition kernel was determined from the broadband luminosity images in the same manner. The lift-off height was defined as the lower edge of the flame in the thresholded OH* CL images, the leading edge of the flame was the upper edge, as shown in Fig. 3.

Figure 4 shows a sample image series from the Schlieren measurements. The solid line indicates the position of the tip of the jet. The detection of the jet tip enabled a qualitative comparison between the downstream location of the first auto-ignition event and the downstream position of the jet tip. The velocity of the jet tip directly after the jet exits the nozzle was also estimated from these images.
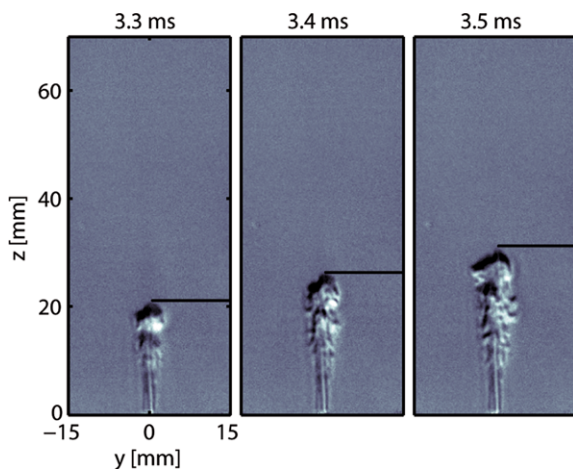

Fig. 4 Sample Schlieren image sequence demonstrating the detection of the tip of the injected methane jet. The times at the top of the frames represent the time after the trigger pulse for the valve opening

3 Results and discussion

The procedure for the measurements was as follows: the hydrogen/air flat flame was operated for at least 15 min in order to achieve thermal equilibrium of the burner. The laser was running continuously. A trigger pulse started a fixed-length recording of the high-speed cameras and after a 2 ms delay the solenoid valve was opened. For the PLIF/CL measurements, the OH* CL camera and the broadband luminescence camera were triggered simultaneously, 1 μs after the PLIF camera. For the Schlieren/CL measurements, all cameras were triggered simultaneously. In order to achieve a statistically significant number of recording sequences, the camera memory was segmented into 80 blocks of 100 frames each (40 blocks of 200 frames for the 10 kHz measurements). The measurements were repeated at a rate of 0.5 Hz to prevent influences from the preceding run on the current run. Since the tip of the nozzle became relatively hot and was cooled by the flowing methane jet, the first recording loop of an acquisition series was not included in the data evaluation in order to achieve comparable boundary conditions for all data runs.

The exit velocity of the jet, estimated from the Schlieren images, was on the order of 16 m s^{-1} for the startup. The velocity of the steady-state jet was determined from the flow rate measured by the Coriolis flow meter and was 100 m s^{-1}. The lift-off height of the flame stabilized quickly, i.e. 0.4 ms after the onset of auto-ignition or 2.3 ms after the jet exiting the fuel nozzle, as will be discussed below. It can be concluded that the flow rate of the jet reached steady-state conditions quickly too, since the lift-off height is quite sensitive to the exit velocity of the jet [25].

In Fig. 5, a typical time sequence of an auto-ignition event is shown that was recorded simultaneously with OH PLIF, OH* CL and broadband flame luminosity imaging. The x- and y-axes span the coordinate system in the plane of the burner (radial directions) with the x-axis being parallel and the y-axis being perpendicular to the laser sheet. The z-axis marks the axial direction. The origin of the coordinate system is in the center of the tip of the fuel nozzle. The signal intensity color scale is given on the right-hand side of the images, and the intensity of each image is normalized by the maximum signal intensity of the complete image series. The color bar for the PLIF and CL measurements is set to a maximum of 0.5 and the color bar of the luminosity measurements is set to a maximum of 0.1 in order to enable the reader to better identify low-count-level features. The reference time starts with the trigger pulse for the valve opening (which is at $t = -2.9$ ms). Note also that the methane jet does not exit the injector tube immediately after the trigger pulse, but with a delay of approximately 2.9 ms, as was determined with high-speed Schlieren imaging as will be discussed below.
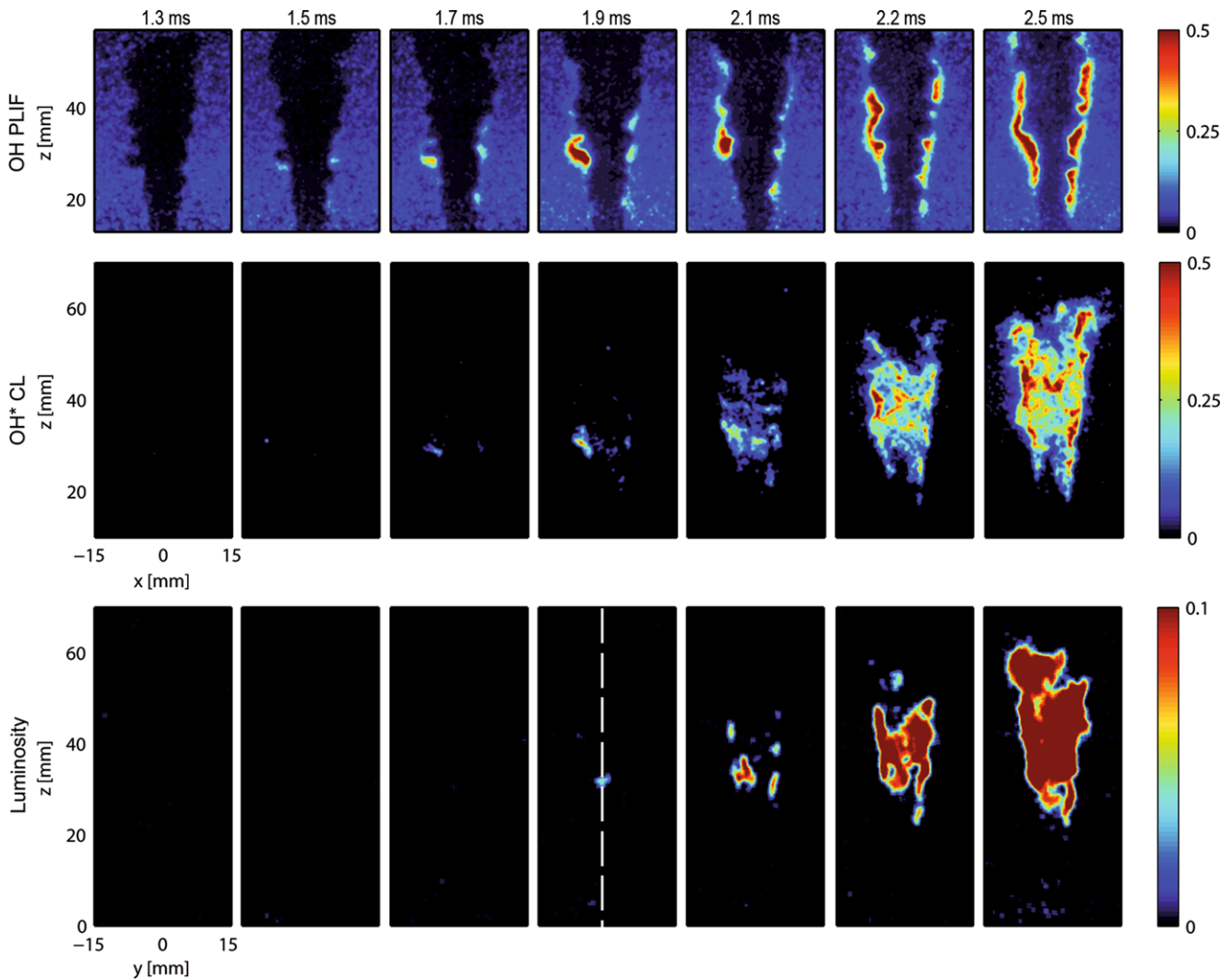
Fig. 5 Image sequence from an auto-ignition event recorded simultaneously with OH PLIF, OH* chemiluminescence and flame luminosity imaging perpendicular to the OH* chemiluminescence. The *dashed line* in the luminosity image at 4.8 ms indicates the position of the laser sheet

In the OH PLIF image at $t = 1.3$ ms a homogeneous distribution of OH (blue region), which represents the hot exhaust gas of the flat flame, can be seen on the left and right sides of the cold inflowing jet (black region). The higher signal intensity at the bottom of the image is probably a result of superequilibrium OH that is formed in the reaction zone of the flat flame. It has a lifetime of several milliseconds [44] and propagates downstream several millimeters before it reaches chemical equilibrium. The OH from the coflow is disappearing as the methane is injected and mixes with the coflow due to the rapid temperature drop and the OH depletion by chemical reactions.

The tip of the jet can be seen at the top edge of the first image frame and is at an axial location of $z = 55$ mm at $t = 1.3$ ms. The diameter at the bottom edge, i.e. 13 mm above the nozzle, deduced from the OH PLIF image, is approximately 6 mm. In the next frame, at $t = 1.5$ ms, a rise in

the LIF signal intensity can be seen at an axial location of approximately 28 mm, left and right of the inflowing jet, which represents the formation of ignition kernels. The kernel on the left-hand side of the jet forms in a bulge of the inflowing jet and grows in both axial and radial size as well as intensity until approximately $t = 1.9$ ms. On the right-hand side, another kernel appears but the PLIF intensity of both kernels remains small. After $t = 1.9$ ms several other ignition kernels can be seen in the PLIF images that finally merge to a closed reaction layer. The downstream convection of the flame kernels is significantly slower than the flame kernel growth. The same kernel can also be seen in the OH* CL images, starting at $t = 1.7$ ms and in the broadband luminosity images, starting at $t = 1.9$ ms. The delayed appearance of the kernel in the broadband luminosity image is explained by the lower sensitivity of the non-intensified camera used for this measurement. Note that the ignition kernel forms di-

Fig. 6 Four ignition events showing the tendency of the ignition kernel to form inside a bulge of the inflowing jet. The same color bar as in Fig. 5 is used
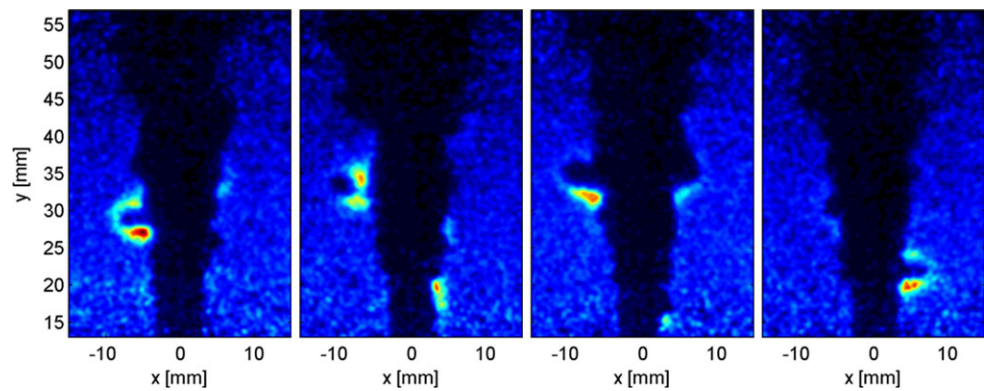
rectly in the laser light sheet, as can be seen from the broadband luminosity images. Thus, the OH PLIF images display the generation of a flame kernel and not the convection or expansion of an OH filament into the laser light sheet.

At $t = 2.1$ ms several other ignition kernels can be seen in the OH PLIF image that form at the periphery of the jet and grow rapidly in size and intensity afterwards. The formation of several additional ignition kernels is also visible in the OH* CL and broadband luminosity images. Also, ignition kernels are visible at a lower axial location than the first observed ignition kernel. After their first occurrence, the kernels grow rapidly in size and finally merge to a continuous flame front. From the OH* CL images it is visible that the region of heat release is not equally distributed and strongly structured.

In order to investigate whether the occurrence of the first auto-ignition kernel in a bulge is random or symptomatic, further sequences were analyzed. As seen from Fig. 5, the line-of sight averaging techniques are not suitable for this purpose and only the OH PLIF images exhibit the required spatial resolution. Measurements where the first auto-ignition occurred inside the laser light sheet were selected and Fig. 6 shows four examples of these single-shot PLIF frames. In all the cases the auto-ignition kernel forms inside a bulge of the inflowing jet. This behavior is typical for the majority of the observed ignition events. The reason for this observation could be the fact that the scalar dissipation rate is expected to be lower at regions where the isoline of the most reactive mixture fraction χ_{mr} is concave to the air [8] and, according to direct numerical simulation (DNS) with single-step chemistry [45] and detailed chemistry [46], auto-ignition preferentially takes place at locations of minimal scalar dissipation rate.

Important parameters for comparison of the auto-ignition dynamics for different coflow conditions are the ignition time, i.e. the time between the trigger for the valve opening and the first appearance of an auto-ignition kernel, and the ignition location, i.e. the height of the first detected auto-ignition kernel above the nozzle. Two methods for detecting the ignition time will be described below.
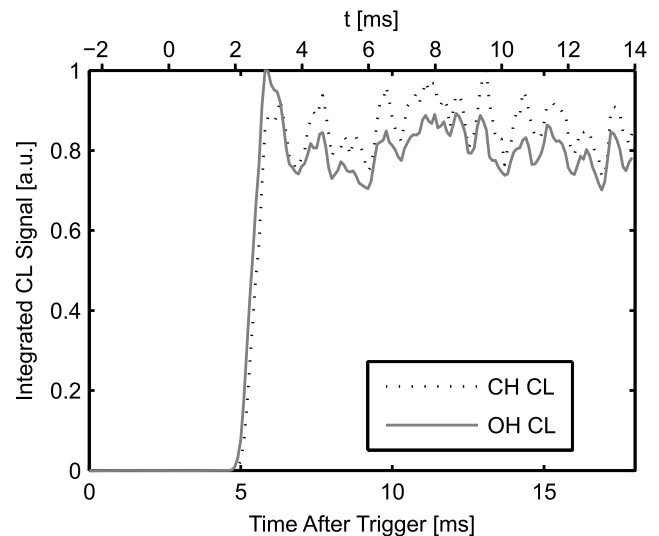

Fig. 7 Integrated OH* and CH* chemiluminescence for one ignition event. t represents the time after the jet exited the fuel nozzle

Figure 7 shows the integrated OH* and CH* CL (integration area: $z = 10$ to 70 mm, $x = -15$ to 15 mm) of one ignition event. Note that this is not the same ignition event as shown in Fig. 5, but one that was recorded with temporal resolution of 10 kHz with simultaneous Schlieren imaging of the jet. When looking at the OH* CL, a very low signal level, representing the background, can be seen until 1.8 ms after the jet exiting the fuel nozzle. Starting at $t = 1.9$ ms, the signal intensity rises rapidly and reaches its maximum at $t = 2.9$ ms. The CH* CL follows the same behavior at the beginning, but occurs approximately 0.1 ms later, which is due to the slower reaction path that leads to the formation of CH* [47, 48]. Note also that the maximum of CH* CL is reached later in the image sequence than that of OH*. After stabilization of the jet flame, both OH* and CH* do not stay at a constant level but fluctuate by a standard deviation of 5 % for the OH* CL and by a standard deviation of 6 % for the CH* CL.

In Fig. 8, the temporal evolution of the position of the tip of the methane jet and the development of the jet flame
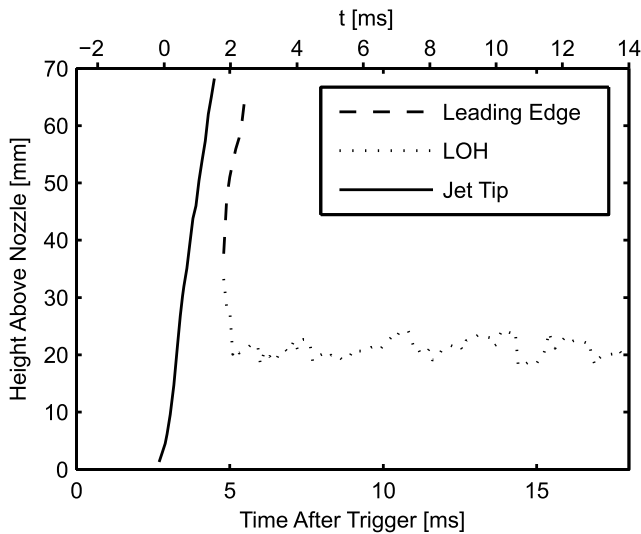
Fig. 8 Time series of the temporal evolution of the position of the tip of the injected methane jet, and the leading edge and lift-off height (LOH) of the igniting jet flame, as detected with the OH* chemiluminescence. t represents the time after the jet exited the fuel nozzle

is shown for the same auto-ignition event as presented in Fig. 7. The leading edge and lower edge of the flame kernel are deduced from the thresholded OH* CL images, as described above. In the measurement sequence shown, the first auto-ignition kernel is observed at $t = 1.9$ ms at approximately 35 mm above the nozzle. At this time, the leading edge of the fuel jet is already out of the field of view of the Schlieren camera, i.e. higher than 70 mm above the nozzle. The leading edge of the fuel jet passes the region of the first observed auto-ignition approximately 1.2 ms before the auto-ignition actually occurs. The leading edge of the igniting jet propagates out of the field of view quickly and reaches a height greater than 70 mm above the nozzle at approximately 2.7 ms. The lower edge of the ignition kernel reaches the mean lift-off height of the stably burning jet flame approximately 0.3 to 0.4 ms after the ignition kernel is first observed. As was shown previously, the upstream expansion of the flame area, as presented in Fig. 8, is not only due to flame propagation but also due to the formation of multiple ignition kernels at lower axial locations than the first ignition kernel. After reaching its stable position, the lift-off height stays approximately constant, but is still fluctuating about its mean value. It should be noted that the downstream flame kernel expansion is not directly correlated to the jet expansion as might be assumed from the similar slopes of the curves in Fig. 8. Two different mechanisms are responsible for the two phenomena. The velocity of the jet tip, as visualized by evaluation of the Schlieren measurements, yields the peak velocity of the jet, i.e. in the center region of the jet. The flame expansion takes place on a circumference at the interface between the fuel jet and the coflow. Since the stoichiometric mixture fraction in the case

presented here is only $f_{\text{stoich}} = 0.0284$ and the most reactive mixture fraction is even lower than this [8], the fluid velocity at the region of flame expansion should be close to the coflow velocity, if conservation of momentum is assumed to get a rough estimate. Therefore the flame kernel growth and downstream expansion seen in Fig. 8 can be the result of either flame propagation (and not ignition kernel convection) or of multiple ignition kernels that occur at almost the same time. The latter reason is the more probable one, since the occurrence of multiple ignition kernels right after the formation of the first ignition kernel was observed in many of the measurement sequences, although it sometimes is difficult to differentiate between different ignition kernels in the CL images due to the line-of-sight integration of this measurement technique.

The analysis of 158 individual auto-ignition events for the operational parameters as described above yielded an average auto-ignition time (determined by thresholding the OH* CL images) of 1.72 ms after the jet exited the fuel nozzle with a standard deviation of 0.11 ms. The mean ignition time that was determined by integrating the total OH* CL was 1.73 ms with a standard deviation of 0.10 ms (corresponding to 6.4 %). It should be noted that for 21 out of the 158 analyzed ignition events both methods yielded different ignition times. For all those events, the difference in ignition times was no more than one frame or 0.2 ms. As was described above, the statistics of the ignition time is not influenced by this and both methods are well suited to determine the ignition time. Since only the thresholding of the OH* CL frames enables an analysis of the spatial location of the auto-ignition, this method is preferred by the authors.

In Fig. 9, a histogram of the detected auto-ignition heights is shown. The location of the detected auto-ignition heights stretches from 13.5 to 41.8 mm above the nozzle. The mean height of the first observed auto-ignition kernel was 25.88 mm above the nozzle with a standard deviation of 5.53 mm (corresponding to 21.4 %). The mean lift-off height of the jet flame for all 158 analyzed measurements was 19.27 mm with a standard deviation of 1.02 mm. This was determined by first evaluating the mean lift-off height for the steady-state jet flame for all 158 measurements and then calculating the average of the mean lift-off heights. It can be seen that the mean location of the first observed auto-ignition is approximately 6 mm further downstream than the stabilization height of the lifted jet flame. The question arises by what mechanism the lifted flame is stabilized and how the upstream propagation of the auto-ignition kernel by ≈ 6 mm is explained. Measurements at a lower coflow temperature of $T = 1613$ K resulted in a mean auto-ignition height of $z = 32.9$ mm and a mean stabilization height of the lifted jet flame of $z = 35$ mm [49]. The close proximity of those numbers led to the assumption that auto-ignition is the
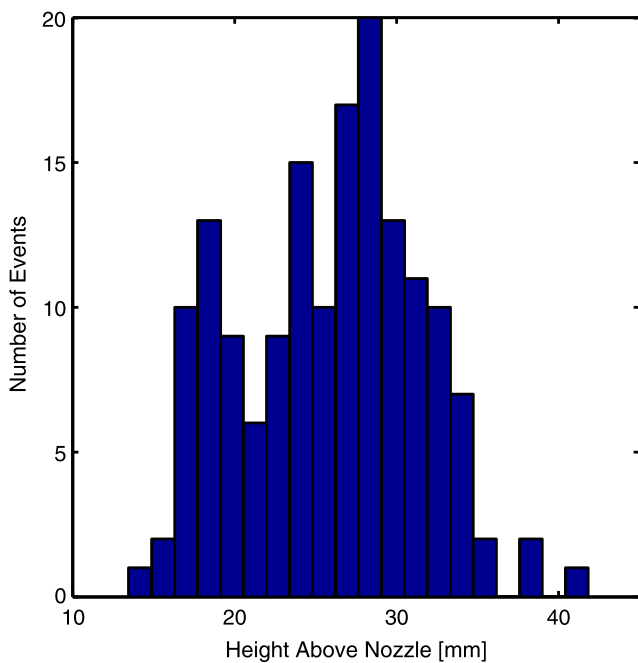
Fig. 9 Histogram of the detected auto-ignition heights above the nozzle
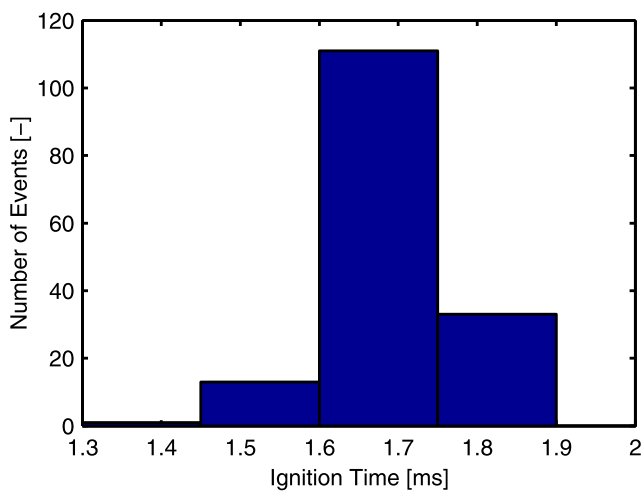

Fig. 10 Histogram of the detected auto-ignition times. The bin width was chosen equal to the time separation between two successive OH* images (0.2 ms)

main mechanism for the stabilization of the lifted flame, in agreement with the findings of other studies [8]. The difference in height ($\Delta z = 6$ mm) measured in the current study and the upstream movement of the flame after ignition however are most probably explained by the occurrence of several ignition kernels below the location of the first ignition kernel a few hundred microseconds after the first ignition kernel and not by edge-flame propagation.

In order to compare the randomness of the ignition kernel location shown in Fig. 9, the histogram of detected auto-ignition times is shown in Fig. 10. The mean detected

auto-ignition time is 1.72 ms, the most probable ignition time 1.7 ms. From the good reproducibility of the ignition time it can be concluded that the experimental configuration has a high run-to-run repeatability. However, it remains unclear why the auto-ignition height has a much larger scatter, at least on a percentage basis. The definition of the auto-ignition time used here might be inappropriate for this comparison, because the portion from the fuel flow involved in the first ignition exits the nozzle significantly later than the leading edge of the jet. Further, the history of the influence of turbulent velocity fluctuations, mixing and scalar dissipation rate on the time and location of auto-ignition events cannot be reconstructed from these measurements. However, similar observations have been made by Wright et al. [50], who investigated the auto-ignition of n-heptane sprays at high pressure. Similarly, the auto-ignition time was highly reproducible, while the auto-ignition sites were distributed over a wider spatial range.

Figure 11 shows an image sequence of OH* CL, starting at 200 ms after the trigger pulse for the valve opening (i.e. 192.6 ms after the first auto-ignition for this measurement sequence). This is well after a stabilized jet flame established. The mean lift-off height is 20.4 mm with a standard deviation of 1.8 mm. The minimum lift-off height of this sequence is 13.8 mm and the maximum lift-off height is 26.8 mm, based on 2500 consecutive evaluated image frames. It should be noted that the individual frames are not statistically independent; however, the averaged run is long enough (0.5 s) for the statistics to compile. An auto-ignition kernel is visible forming well below the flame base at approximately 17 mm above the nozzle. The kernel grows in size and intensity, and the centroid of the kernel propagates downstream. Finally, approximately 0.8 to 1.0 ms after the auto-ignition kernel begins to form, it merges with the flame base of the jet flame. This behavior is observed quite frequently in a given measurement sequence for certain coflow conditions, i.e. with coflow temperatures below 1700 K. For the setup in the present study, the average value of the height above the nozzle of the first observed auto-ignition kernel and the average lift-off height of the steady-state jet flame differ quite significantly. However, shortly after the first auto-ignition kernel it is frequently observed that several other auto-ignition kernels occur at different axial locations. Also, if not the average height of the first observed auto-ignition is taken into account, but the full distribution of the measured values is considered, the range of auto-ignition heights overlaps well with the range of the stabilization heights of the steady-state lifted jet flame. Therefore, it can be concluded that auto-ignition plays a significant role in the stabilization of the steady-state lifted jet flame.
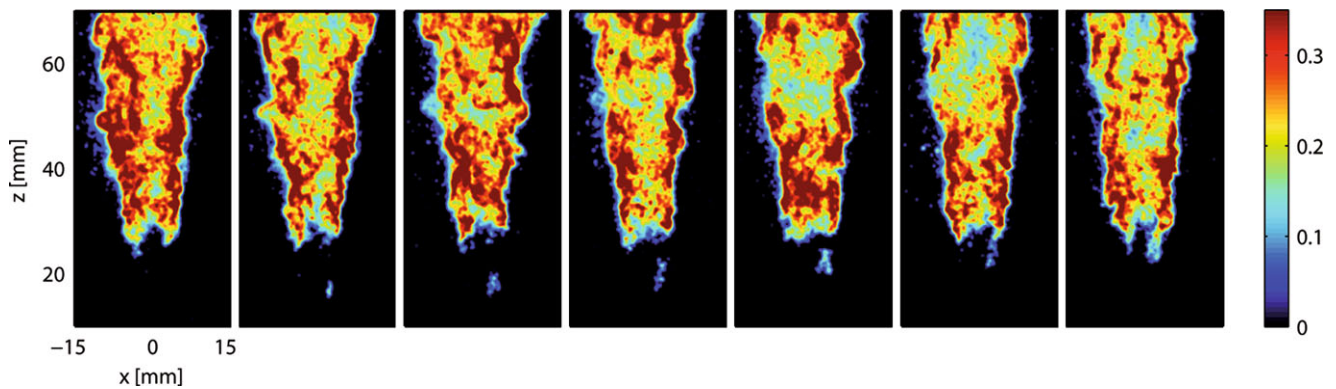
Fig. 11 OH* chemiluminescence image series of the dynamics of the stably burning jet flame and the formation of auto-ignition islands below the flame base. Time between frames is 0.2 ms

4 Conclusions

High-speed laser and imaging techniques have been applied to study the auto-ignition of a pulsed methane jet in a vitiated coflow. Simultaneous OH planar laser-induced fluorescence (PLIF), OH* chemiluminescence (CL) and broadband flame luminosity measurements have been performed at a sustained repetition rate of 5 kHz as well as simultaneous OH* and CH* CL measurements in combination with Schlieren imaging at a sustained repetition rate of 10 kHz. A large number of auto-ignition events has been recorded in order to gain statistics about the ignition time and the location of the first ignition kernel. While the OH PLIF and the OH* CL camera had the same imaging plane, the broadband luminosity camera looked at the jet from the direction of the laser sheet in order to gain three-dimensional information about the location of the first ignition kernel. Only events where the first ignition kernel formed inside the plane of the laser light sheet were included in a further analysis of the OH PLIF measurements. In this way, the high spatial resolution of the PLIF technique could be exploited for the characterization of auto-igniting flame kernels.

It was shown that both the detection of individual ignition kernels and the use of the integrated OH* CL signal are viable methods for determining the ignition time. The detailed analysis of representative auto-ignition events where the first kernel lay inside the laser light sheet has shown that the first auto-ignition tends to form inside bulges of the inflowing jet where the scalar dissipation rate is expected to be lower than in other regions of the mixing layer. The ignition kernels always formed well below the leading edge of the inflowing fuel jet in the periphery of the jet. Often, several ignition kernels appeared almost simultaneously and merged rapidly to a connected flame sheet. A statistical analysis of 158 auto-ignition events yielded an average auto-ignition height of 25.9 mm above the nozzle and a typical ignition time of 1.72 ms after the jet exited the fuel nozzle. The mean value for the lift-off height for the stable flame

was 19.3 mm above the nozzle. While the downstream location of the auto-ignition kernels was distributed over a relatively wide range, the auto-ignition time was found to be almost constant. The observation that the flame stabilized well below the location of the first auto-ignition is most likely explained by further auto-ignition events upstream of that location and not by edge-flame propagation.

References

1. A. Koch, C. Naumann, W. Meier, M. Aigner, in *Proc. ASME Turbo Expo*, 2005, Paper No. GT2005-68405
2. F. Güthe, J. Hellat, P. Flohr, J. Eng. Gas Turbines Power **131**, 021503 (2009)
3. J.M. Fleck, P. Griebel, A.M. Steinberg, M. Stöhr, M. Aigner, A. Ciani, in *Proc. ASME Turbo Expo*, 2010, Paper No. GT2010-22722
4. J. Fleck, P. Griebel, A.M. Steinberg, M. Stöhr, M. Aigner, J. Eng. Gas Turbines Power **134**, 041502 (2012)
5. I. Boxx, M. Stöhr, C. Carter, W. Meier, Combust. Flame **157**, 1510 (2010)
6. J. de Vries, E. Petersen, Proc. Combust. Inst. **31**, 3163 (2007)
7. T. Lieuwen, V. McDonell, D. Santavicca, T. Sattelmayer, Combust. Sci. Technol. **180**, 1169 (2008)
8. E. Mastorakos, Prog. Energy Combust. Sci. **35**, 57 (2009)
9. L. Spadaccinia, M. Colket III, Prog. Energy Combust. Sci. **20**, 431 (1994)
10. G. Cho, D. Jeong, G. Moon, C. Bae, Energy **35**, 4184 (2010)
11. C. Markides, E. Mastorakos, Proc. Combust. Inst. **30**, 883 (2005)
12. C.N. Markides, E. Mastorakos, Flow Turbul. Combust. **86**, 585 (2011)
13. S.S. Patwardhan, K.N. Lakshmisha, Int. J. Hydrog. Energy **33**, 7265 (2008)
14. K.G. Gupta, T. Echekki, Combust. Flame **158**, 327 (2011)
15. R.L. Gordon, A.R. Masri, E. Mastorakos, Combust. Flame **155**, 181 (2008)
16. T. Mosbach, R. Sadanandan, W. Meier, R. Eggels, in *Proc. ASME Turbo Expo*, 2010, Paper No. GT2010-22625

17. C. Fajardo, V. Sick, Exp. Fluids **46**, 43 (2009)
18. C. Heeger, B. Böhm, S. Ahmed, R. Gordon, I. Boxx, W. Meier, A. Dreizler, E. Mastorakos, Proc. Combust. Inst. **32**, 2957 (2009)
19. R. Sadanandan, D. Markus, R. Schießl, U. Maas, J. Olofsson, H. Seyfried, M. Richter, M. Aldén, Proc. Combust. Inst. **31**, 719 (2007)
20. W. Meier, I. Boxx, C. Arndt, M. Gamba, N. Clemens, J. Eng. Gas Turbines Power **133**, 021504 (2011)
21. E. Oldenhof, M.J. Tummers, E.H. van Veen, D.J.E.M. Roekaerts, Combust. Flame **159**, 697 (2012)
22. G. Bruneaux, Oil Gas Sci. Technol. **63**, 461 (2008)
23. G. Fast, D. Kuhn, A. Class, U. Maas, Combust. Flame **156**, 200 (2009)
24. R. Cabra, T. Myhrvold, J. Chen, R. Dibble, A. Karpetis, R. Barlow, Proc. Combust. Inst. **29**, 1881 (2002)
25. R. Cabra, J.Y. Chen, R. Dibble, A. Karpetis, R. Barlow, Combust. Flame **143**, 491 (2005)
26. B. Dally, A. Kerpetis, R. Barlow, Proc. Combust. Inst. **29**, 1147 (2003)
27. Z. Wu, A.R. Masri, R.W. Bilger, Flow Turbul. Combust. **76**, 61 (2006)
28. P.R. Medwell, P.A. Kalt, B.B. Dally, Combust. Flame **148**, 48 (2007)
29. B. Choi, K. Kim, S. Chung, Combust. Flame **156**, 396 (2009)
30. B. Choi, S. Chung, Combust. Flame **157**, 2348 (2010)
31. E. Oldenhof, M.J. Tummers, E.H. van Veen, D.J.E.M. Roekaerts, Combust. Flame **157**, 1167 (2010)
32. E. Oldenhof, M.J. Tummers, E.H. van Veen, D.J.E.M. Roekaerts, Combust. Flame **158**, 1553 (2011)
33. S.H. Kim, K.Y. Huha, B. Dally, Proc. Combust. Inst. **30**, 751 (2005)
34. F. Christo, B. Dally, Combust. Flame **142**, 117 (2005)
35. R.R. Cao, S.B. Pope, A.R. Masri, Combust. Flame **142**, 438 (2005)
36. R. Gordon, A. Masri, S. Pope, G. Goldin, Combust. Theory Model. **11**, 351 (2007)
37. P. Domingo, L. Vervisch, D. Veynante, Combust. Flame **152**, 415 (2008)
38. S.S. Patwardhan, S. De, K.N. Lakshmisha, B.N. Raghunandan, Proc. Combust. Inst. **32**, 1705 (2009)
39. C.S. Yoo, R. Sankaran, J.H. Chen, J. Fluid Mech. **640**, 453 (2009)
40. M. Ihme, Y.C. See, Combust. Flame **157**, 1850 (2010)
41. C. Morley, Gaseq—a chemical equilibrium program for Windows
42. Manufacturer information
43. S. Prucker, W. Meier, W. Stricker, Rev. Sci. Instrum. **65**, 2908 (1994)
44. R. Sadanandan, M. Stöhr, W. Meier, Appl. Phys. B **90**, 609 (2008)
45. E. Mastorakos, T.A. Baritaud, Combust. Flame **109**, 198 (1997)
46. R. Hilbert, D. Thévenin, Combust. Flame **128**, 22 (2002)
47. G.P. Smith, J. Luque, C. Park, J.B. Jeffries, D.R. Crosley, Combust. Flame **131**, 59 (2002)
48. J.M. Hall, M.J.A. Rickard, E.L. Petersen, Combust. Sci. Technol. **177**, 455 (2005)
49. W. Meier, C. Arndt, J. Gounder, I. Boxx, K. Marr, in *Proc. 23rd ICDERS* (2011), paper no. 90
50. Y.M. Wright, O.-N. Margari, K. Boulouchos, G. De Paola, E. Mastorakos, Flow Turbul. Combust. **84**, 49 (2010)